Atmospheric Research 325 (2025) 108214

Contents lists available at ScienceDirect

Atmospheric Research

journal homepage: www.elsevier.com/locate/atmosres

Evaluation of convectively coupled Kelvin waves in CMIP6 coupled climate models

Xianpu Ji [a,b], Tao Feng [a,b,*], Ping Huang [c], Xuhua Cheng [a,b], Jianhuang Qin [a,b], Ben Yang [d]

[a] Key Laboratory of Marine Hazards Forecasting, Hohai University, Nanjing, 210024, China
[b] College of Oceanography, Hohai University, Nanjing, 210024, China
[c] Center for Monsoon System Research, Institute of Atmospheric Physics, Chinese Academy of Sciences, Beijing, 100017, China
[d] School of Atmospheric Sciences, Nanjing University, Nanjing, 210023, China

ARTICLE INFO

Dataset link: https://pcmdi.llnl.gov/CMIP6/, https://cds.climate.copernicus.eu/datasets

Keywords:
Kelvin wave
CMIP6
Precipitation
Climate model

ABSTRACT

Although the coupled climate models experienced significant improvement over the past few decades, they continue to suffer from common biases in the representations of tropical intraseasonal to synoptic variabilities interacting with organized tropical convection. This study presents a quantitative assessment of convectively coupled Kelvin waves (CCKWs) over the tropical ocean, as simulated by 20 coupled climate models participating in the Coupled Model Intercomparison Project Phase Six (CMIP6). The standard deviation of filtered daily precipitation anomalies as well as the spatial–temporal spectrum are used to evaluate the performance of the amplitude of eastward propagating CCKWs. By comparing the observations from the Global Precipitation Climate Program, CMIP6 models are classified into good and poor categories. Good models can well simulate the spectral coverage and the spatial characteristics of CCKWs, while poor models underestimate the CCKWs' activity. Good models generally illustrate the seasonal evolution of CCKWs, with non-negligible deviations during boreal early spring. In contrast, poor models failed to reproduce the seasonal migration between the Southern and Northern hemispheres of CCKWs. Moreover, both good and poor models exhibit remarkable biases in CCKW activity over the Maritime Continent and equatorial South America. The simulation bias of CCKWs is correlated to the strength of the background precipitation rate in association with the North Pacific intertropical convergence zone. Further analysis suggests that the CCKWs simulation skill is positively correlated to the convective precipitation fraction which is related to convective parameterization schemes.

1. Introduction

Convectively coupled Kelvin waves (CCKWs) are eastward-propagating equatorial waves that share the fundamental characteristics of classical equatorial Kelvin waves (Matsuno, 1966; Lindzen, 1967), but are modified by organized moist convection (Wolding et al., 2020; Weber et al., 2021). These waves are critical in modulating tropical weather systems and significantly contribute to the variability of tropical rainfall and convection (Cheng et al., 2023; Lubis and Jacobi, 2015; Kim and Alexander, 2013; Roundy and Frank, 2004). Additionally, CCKWs are associated with extreme precipitation events over the equatorial regions (Senior et al., 2023; Lubis and Respati, 2021; Peyrillé et al., 2023), tropical cyclogenesis (Schreck, 2015; Frank and Roundy, 2006; Bessafi and Wheeler, 2006), and the Madden–Julian Oscillation (MJO) (Neena et al., 2022; Kikuchi et al., 2018; Roundy, 2012, 2008). The vertical propagation of CCKWs facilitates troposphere–stratosphere exchange by transporting zonal momentum upward (Yang et al., 2011), playing a crucial role in simulating the quasi-biennial oscillation (QBO) (Wang et al., 2023, 2025; Garfinkel et al., 2022). Therefore, a detailed evaluation of the CCKWs in advanced earth system models is essential for predicting tropical weather changes and coping with extreme weather events brought about by climate change.

The observational characteristics of CCKWs in the equatorial troposphere, including their structure, dispersion relationship, and propagation features, have been extensively studied (Wheeler et al., 2000; Kiladis et al., 2009). These observed waves exhibit numerous similarities to their theoretical counterparts, including near non-dispersive feature, eastward propagation, and a westward tilt with increasing height (Wheeler and Kiladis, 1999; Straub and Kiladis, 2003; Kiladis et al., 2009). The circulation associated with CCKWs is primarily influenced by zonal winds in the vicinity of the equator (Kiladis et al., 2009; Wang and Li, 2017). Generally, CCKWs propagate along the

* Corresponding author at: College of Oceanography, Hohai University, Nanjing, 210024, China.
E-mail address: fengtao@hhu.edu.cn (T. Feng).

https://doi.org/10.1016/j.atmosres.2025.108214
Received 13 February 2025; Received in revised form 29 April 2025; Accepted 12 May 2025
Available online 28 May 2025

equator with eastward phase speeds ranging from 10 to 20 m s^{-1}, exhibiting planetary scales with zonal wavelengths between 3000 and 7000 km, corresponding approximately to zonal wavenumbers 6 to 13, respectively (Gruber, 1974; Takayabu, 1994; Straub and Kiladis, 2002, 2003; Kiladis et al., 2009; Lawton and Majumdar, 2023). However, the phase speed is notably slower than those of classical (dry) Kelvin waves, that is possibly attributed to the coupling with moist convection and the background easterly (Kiladis et al., 2009; Dias and Kiladis, 2014; Tulich and Kiladis, 2021; Herman et al., 2016). Moreover, the understanding of the convective coupling process remains limited, which could result in biases when simulating CCKWs in earth system models. For instance, Wang and Li (2017) conducted a comprehensive evaluation of CCKWs in the Coupled Model Intercomparison Project Phase Five (CMIP5) coupled models, finding a prevalent bias where simulations overestimated CCKWs activity in the equatorial South Pacific. Similarly, some earth system models, e.g., CAMS-CSM, showed unrealistic spatial distribution of wave activities, with enhanced CCKWs drifting from the Northern Hemisphere to the Southern Hemisphere (Wang et al., 2019). These persistent biases highlight the challenges encountered by the earth system model in accurately modeling CCKWs.

In addition to the planetary-scale characteristics, the spatial distributions and multiscale variations of CCKWs are also examined. Previous studies have suggested that CCKWs activity exhibits maximum interannual variance at the equator during boreal winter, while its intensity persists throughout the season (Wang and Chen, 2016). Some studies found that the seasonal activity of CCKWs mirrors the seasonal cycle of Intertropical Convergence Zone (ITCZ), implying a relationship between the meridional migrations of CCKWs and ITCZ (Lubis and Jacobi, 2015; Huang and Huang, 2011). As a principal mode of interannual variability within the ocean–atmosphere system, the El Niño-Southern Oscillation (ENSO) significantly influences CCKWs. This influence occurs mainly through ENSO-induced changes in underlying thermal conditions, ambient flow, and the modulation of local and remote forcing, which in turn affect the variability of CCKWs (Wang and Chen, 2016; Yang et al., 2023; Yang and Hoskins, 2013). Therefore, it is necessary to assess the representation of CCKWs in the latest generation of Earth system models.

In recent decades, Earth system models have made notable progress in simulating equatorial waves, including the MJO. Compared to earlier CMIP3 and high-resolution models (Lin et al., 2006; Huang et al., 2013; Yang et al., 2009; Straub et al., 2010; Hung et al., 2013), CMIP5 models exhibit enhanced intraseasonal variance, more realistic phase speeds, and stronger signals in key equatorial wave modes, such as Kelvin waves, equatorial Rossby (ER) waves, and eastward inertio-gravity (EIG) waves (Hung et al., 2013; Wang and Li, 2017). In CMIP3 models, only about half of the 14 participating models exhibit convectively coupled equatorial wave (CCEW) signals, with generally weak variances for most wave modes except the EIG wave (Yang et al., 2009; Lin et al., 2006). MJO-related variance in models lacks a distinct spectral peak, instead appearing as part of a broad, undifferentiated spectrum (Hung et al., 2013). Antisymmetric modes such as mixed Rossby-gravity (MRG) waves and tropical depression-type (TD-type) waves relevant to tropical cyclone genesis are consistently underestimated (Huang et al., 2013). CMIP6 models demonstrate further improvement, simulating equatorial wave spectra that are quantitatively similar to observations. However, challenges remain: the amplitudes of MJO and Kelvin waves across the spectrum are still underestimated, while ER wave signals tend to be overestimated (Bartana et al., 2023; Ahn et al., 2020; Le et al., 2021). Thus, despite substantial advancements across CMIP phases, accurately representing the convection–wave coupling remains a major challenge in current climate models.

Despite the significant influence of CCKWs on weather and climate systems, the mechanisms driving convection–waves interaction remain a challenge, potentially resulting in biases in the intensity of simulated CCKWs. Various theories have been proposed to elucidate the internal dynamics of CCKWs, particularly concerning instability mechanisms. Early theories, such as wave instability of the second kind (Wave-CISK) (Hayashi, 1970; Yamasaki, 1969; Lindzen, 1974), wind-induced surface heat exchange (WISHE) (Emanuel, 1987; Neelin et al., 1987), stratiform instability (Mapes, 2000; Kuang, 2008), offer different perspectives on the mechanisms driving CCKWs. These mechanisms are generally categorized into two main schools: one concentrating on the first baroclinic mode and the other on the second baroclinic mode, both aimed at explaining the observed horizontal scales of the waves. Recent studies have introduced moisture-vortex instability (Mayta and Adames, 2024; Adames and Ming, 2018), emphasizing the role of moisture in the growth of wave instability (Feng et al., 2020a,b). CCKWs are generally classified as gravity-wave-type waves, with their dynamics primarily driven by buoyancy fluctuations (Adames et al., 2019). However, it remains unidentified which vertical mode or instability mechanism is key to destabilizing CCKWs. This uncertainty often leads to the usage of convective parameterization schemes in models, which poorly represent the convection–circulation coupling process in CCKWs. Consequently, such parameterized models may fail to effectively capture CCKWs in earth system simulations (e.g., (Dias et al., 2018)). The simulation of convectively coupled equatorial waves is a critical metric for evaluating model performance, and analyzing biases in these simulations is key to model improvement (Huang et al., 2013). While previous studies have shown that CMIP5 models outperform CMIP3 models in simulating tropical intraseasonal variability (Lin et al., 2006; Meehl et al., 2007; Straub et al., 2010; Huang et al., 2013), they still struggle to accurately reproduce the observed spatial and seasonal characteristics of CCKWs (Huang et al., 2013). As a result, simulating CCKWs remains a significant challenge for enhancing Earth system models.

This study evaluates the performance of state-of-the-art CMIP6 models in simulating CCKWs. Models are classified into two categories based on quantitative metrics that assess the spectrum and spatial distribution of simulated CCKWs. The climatology and variability of CCKWs are then examined, followed by a discussion of potential reasons for simulation biases. The paper is structured as follows: Section 2 describes the participating models, the validation data, and the assessment metrics. Section 3 presents the evaluation of CCKW simulations. Section 4 explores potential sources of bias in the simulations. Finally, Section 5 offers a summary and discussion.

2. Data and methods

2.1. Models

To extract eastward-propagating CCKWs signals, the daily mean precipitation from historical simulations is utilized. A totality of twenty coupled models from the CMIP6 multimodel products are selected to evaluate the simulation of CCKWs under historical scenarios. These models are accessible online at https://pcmdi.llnl.gov/CMIP6/, with Table 1 listing the abbreviations and corresponding institutions. For most models, the r1i1p1f1 ensemble member is used, except for HadGEM3-GC31-LL, MIROC-ES2L, and UKESM1-0-LL, based on available data.

For validation, daily precipitation data are adopted from the Global Precipitation Climatology Project (GPCP) Version 1.3 (Huffman et al., 2001) with a one-degree resolution. To facilitate comparisons between model simulations and observational data, 18 years of simulations (1997–2014) are analyzed, aligning the model outputs with corresponding observational data. This period provides a comprehensive dataset for studying seasonal variability in CCKWs. Sensitivity tests with different analysis periods showed consistent results.

To enhance computational efficiency and ensure comparability, all data were interpolated to a uniform grid with a 2° × 2° horizontal resolution, sufficient to capture the Kelvin wave signal. The first-order conservative remapping schemes were applied for interpolation (Jones, 1999). Additionally, these models' monthly mean precipitation and convective precipitation are used to investigate the possible reasons behind the differences in model performance for simulating CCKWs.

Table 1
List of CMIP6 models and observational data.

	Data	Institution	Horizontal resolution (lat × lon)	Top (levels)	Convection schemes
Observation.	GPCP	National Oceanic and Atmospheric Administration (NOAA), USA	1° × 1° (180 × 360)		
CMIP6	CAMS-CSM1–0	Chinese Academy of Meteorological Sciences (CAMS), China	T106 (160 × 320)	10 hPa (L31)	Nordeng (1994)
	CanESM5	Canadian Centre for Climate Modelling and Analysis (CCCma), Canada	T63 (64 × 128)	1 hPa (L49)	Zhang and McFarlane (1995)
	CESM2	NSF–DOE–NCAR, United States	F09 (192 × 288)	2.25 hPa (L32)	Zhang and McFarlane (1995)
	CESM2-WACCM	NSF–DOE–NCAR, United States	F09 (192 × 288)	4.5×10^{-6} hPa (L70)	Zhang and McFarlane (1995)
	EC-Earth3	Rossby Centre, Swedish Meteorological and Hydrological Institute, European	T_L255 (256 × 512)	0.01 hPa (L91)	Bechtold et al. (2014)
	EC-Earth3-Veg	EC-Earth consortium, Europe	T_L255 (256 × 512)	0.01 hPa (L91)	Bechtold et al. (2014)
	GFDL-CM4	Geophysical Fluid Dynamics Laboratory (GFDL)	C96 (180 × 360)	1 hPa (L33)	Zhao et al. (2018)
	GFDL-ESM4	National Oceanic and Atmospheric Administration (NOAA), United States	C96 (180 × 360)	1 hPa (L49)	Zhao et al. (2018)
	HadGEM3-GC31-LL	Met Office Hadley Centre, UK	N96 (144 × 192)	85 km (L85)	Gregory and Rowntree (1990)
	INM-CM4–8	Institute for Numerical Mathematics (INM), Russia	2° ×1.5° (120 × 180)	sigma = 0.01 (L21)	Betts (1986)
	INM-CM5–0	Institute for Numerical Mathematics (INM), Russia	2° ×1.5° (120 × 180)	sigma = 0.0002 (L73)	Betts (1986)
	IPSL-CM6A-LR	Institut Pierre Simon Laplace (IPSL), France	N96 (143 × 144)	40 km (L79)	Modified Emanuel (1991)
	MIROC6	Atmosphere and Ocean Research Institute	T85 (128 × 256)	0.004 hPa (L81)	Chikira and Sugiyama (2010)
	MIROC-ES2L	National Institute for Environmental Studies/JAMSTEC, Japan	T42 (64 × 128)	3 hPa (L40)	Chikira and Sugiyama (2010)
	MRI-ESM2–0	Meteorological Research Institute (MRI), Japan	T_L159 (160 × 320)	0.01 hPa (L80)	Yoshimura et al. (2015)
	NESM3	Nanjing University of Information Science and Technology (NUIST), China	T63 (96 × 192)	1 hPa (L47)	Nordeng (1994)
	NorCPM1	NorESM Climate Modeling Consortium, Norway	2° × 2° (96 × 144)	≈2 hPa (L26)	Zhang and McFarlane (1995)
	NorESM2-LM	NorESM Climate Modeling Consortium, Norway	2° × 2° (96 × 144)	3 hPa (L32)	Zhang and McFarlane (1995)
	SAM0-UNICON	Seoul National University (SNU), South Korea	1° × 1° (192 × 288)	≈2 hPa (L30)	Park (2014)
	UKESM1-0-LL	Met Office Hadley Centre, UK	N96 (144 × 192)	85 km (L85)	Gregory and Rowntree (1990)

2.2. Analysis method

2.2.1. Spectral analysis

The spatial–temporal filter is applied to daily precipitation data to extract eastward-propagating CCKWs from both observational data and model simulations. First, the climatology of precipitation within the tropical equatorial belt (25°S–25°N) is removed. Next, a spatial–temporal filter is applied to the precipitation anomalies (Wheeler and Kiladis, 1999). This method has been successfully used in previous studies to extract equatorial wave signals from variables such as outgoing longwave radiation (Wheeler and Kiladis, 1999; Straub and Kiladis, 2002; Horng and Yu, 2024), accumulated precipitation rates from Integrated Multi-satellitE Retrievals for GPM (Fahrin et al., 2024; Senior et al., 2023; Cheng et al., 2023), Tropical Rainfall Measuring Mission (Cho et al., 2004; Chien and Kim, 2023), and brightness temperature (Huang and Huang, 2011; Kiladis et al., 2009). In this study, we assume that the filtered precipitation signals primarily represent CCKWs. As the wave identification method is based on precipitation data, it inherently lacks sensitivity to the dynamical characteristics of dry Kelvin waves that are not coupled with convection. Therefore, any conclusions drawn in this study do not account for the presence or behavior of dry Kelvin waves. The simulation of dry Kelvin by the model may need additional evaluation.

The filter domain is defined based on the observed wavenumber–frequency spectrum concerning the theoretical equatorial Kelvin waves (see Fig. 1). Following Wheeler and Kiladis (1999), we use a broader equivalent depth range (8–90 m) for CCKWs. Among these, CCKWs typically exhibit strong spectral power near 25 m, as shown in several previous studies (Kiladis et al., 2009; Wang et al., 2019; Chien and Kim, 2023). Finally, the filter domain encompasses periods from 3 to 20 days and positive wavenumbers between +2 and +14. To further isolate CCKWs, only spectral components that fall within the theoretical dispersion curves corresponding to equivalent depths of 8–90 m are retained, forming an irregular polygonal region in wavenumber–frequency space (indicated by the green polygon in Fig. 1).

2.2.2. Metrics

To characterize the general features of simulated CCKWs, the standard deviation of precipitation anomalies is used. Specifically, the standard deviation of daily-filtered precipitation anomalies associated with CCKWs is computed for each calendar month to quantify monthly wave activity. The seasonal cycle of wave activity is represented by the long-term mean of the monthly activity (Huang and Huang, 2011).

To evaluate the CMIP6 models, the root mean square error (RMSE), correlation coefficient, standard deviation, and between the simulations and GPCP observations are calculated. A Taylor diagram, which integrates the normalized correlation coefficient, standard deviation, and RMSE, is used for a comprehensive assessment of model performance (Taylor, 2001).

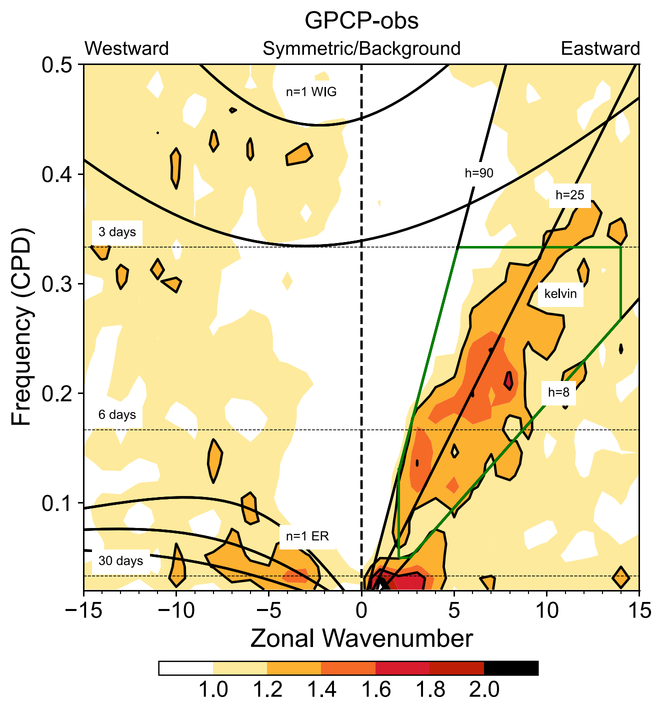

Fig. 1. Symmetric spectral components between 25°N and 25°S obtained from the 1997–2014 GPCP daily precipitation data, shown as the ratio of raw precipitation power to smoothed red noise background spectral power. The thin black solid lines indicate the dispersion curves for various equivalent depths, while the green polygons indicate the filtered range of precipitation.

3. Evaluation of CCKW simulation

3.1. Gross performance of simulated CCKW in spectral analysis

The general performances of CCKWs simulation in CMIP6 models were examined in the spatial–temporal spectrum diagram (Fig. 2). Significant deviations are exhibited in the CCKW simulation in different models. Specifically, 8 out of 20 models (i.e., CAMS-CSM1-0, CESM2-WACCM, EC-Earth3, HadGEM3-GC31-LL, MIROC6, NorCPM1, SAM0-UNICON, and UKESM1-0-LL) their correlation coefficients exceed 0.7, showing better capability in reproducing the spectrum of CCKWs. In contrast, several models, e.g., INN-CM4-8, did not produce the spectrum peak of CCKWs.

Fig. 3 illustrates the horizontal distribution of CCKWs in the equatorial region. Observations reveal that CCKWs are most active over the equatorial North Pacific (Fig. 3a), coinciding with the North Pacific ITCZ. The CCKW activity extends eastward towards South America and westward to the eastern Indian Ocean, with a slight shift toward the equator. The RMSE is calculated by first computing the squared differences between the observed and simulated values at each grid point within the region spanning 0°–360°E and 15°S–15°N, then averaging these squared differences, and finally taking the square root of the result. The results of spatial RMSE suggest that 10 out of the 20 models (i.e., CESM2, CESM2-WACCM, CanESM5, HadGEM3-GC31-LL, MIROC6, MRI-ESM2-0, NorCPM1, NorESM2-LM, SAM0-UNICON, and UKESM1-0-LL) displayed smaller RMSE values below 0.5, indicating better capability of these models for mimicking the spatial pattern of CCKW activity.

Figs. 2 and 3 reveal significant variations among the models in both the spatial–temporal spectra and the horizontal distribution of CCKW activity. While some models perform well in simulating both the spectrum and spatial characteristics of CCKWs, a more detailed analysis is necessary to comprehensively evaluate their performance. To assess the models' ability to reproduce both the spectral and spatial features of CCKWs, the correlation coefficient of the spatial–temporal spectrum and the RMSE of the filtered precipitation's standard deviation are calculated using the widely adopted Taylor diagram. In the Taylor diagram, the reference standard (observations) is represented by the location of the red star. The closer a model's point is to the reference, the smaller the discrepancy between the model and the observations, indicating better performance. Fig. 4 presents the standard deviation, correlation coefficient, and RMSE values for the CMIP6 models, compared to observations in the spectral domain.

Fig. 4 depicts consistent results with those in Fig. 2 and Fig. 3, demonstrating that models closer to the reference point exhibit higher correlation coefficient and lower RMSE (e.g., NorCPM1, SAM0-UNICON, and UKESM1-0-LL). Based on these metrics, five models with higher skill (HadGEM3-GC31-LL, MIROC6, NorCPM1, SAM0-UNICON, and UKESM1-0-LL) and five models with relatively lower skill (CanESM5, GFDL-CM4, INM-CM4-8, INM-CM5-0, and IPSL-CM6A-LR) were selected for further composition (Table 2).

Fig. 5 illustrates the multi-model mean spectrum from good and poor models. The multi-model mean from good models resembles the observational CCKW spectrum with a similar spectrum domain and propagation speed in Fig. 5a. However, the intensity of CCKWs is still weaker than observation, which may be attributed to the lower resolution of the climate models. On the contrary, poor models fail to reproduce distinguishable CCKW signals in Fig. 5b. Dias et al. (2023) observed a slight dispersion of CCKWs, which is evident in Fig. 5c. As the zonal wavenumber increases, the spectral power shifts from the theoretical dispersion curve of Kelvin waves corresponding to an equivalent depth of 90 m to one corresponding to 25 m. This dispersion refers to the eastward group speed that is slightly slower than the Kelvin wave phase. The good models well-simulated the dispersion characteristics of the CCKWs. However, the wave packet moves faster than the Kelvin wave phase as the maximum spectral power shifts to the theoretical dispersion curve with deeper equivalent depth.

3.2. The horizontal distributions of simulated CCKW activity

Fig. 6 illustrates the spatial distribution of CCKW activity over the tropical region, represented by the standard deviation of rainfall over time, comparing selected multi-model averages that were classified as good and poor against observational data. Although both model categories exhibit similar spatial patterns, with CCKW signals extending from the eastern Indian Ocean to the Pacific Ocean, the good models simulate more active CCKWs throughout the Indo-Pacific basin (Fig. 6a), closely matching observations (Fig. 6c). In contrast, the poor models underestimate the intensity of strong CCKWs (Fig. 6b). Observations reveal that CCKW-related precipitation is notably stronger in the boreal hemisphere than in the austral hemisphere (Fig. 6c). However, both categories fail to capture this asymmetry, as the intensity of CCKW activity over the Pacific is similar in both hemispheres (Fig. 6a and 6b). This discrepancy is likely linked to biases in the background field simulations, particularly the well-known double-ITCZ problem in coupled climate models (Wang et al., 2019; Wang and Li, 2017), which will be discussed further. Notably, neither the good nor poor model ensemble averages reproduce the CCKW signals over South America, raising concerns about the models' ability to simulate the evolution of CCKWs across the continent.

Fig. 7 presents the zonal distributions of the standard deviation of CCKWs, averaged over the latitudinal band from 15°S to 15°N. The bottom half represents results based on the GPCP observation (black solid curve), good model averages (red solid curve), and poor model averages (cyan-blue curve). The dashed lines in the upper half indicate simulations in different models. Observational data reveal that, similar to the spatial distribution results shown in Fig. 6, the rainfall maximum exhibits three peaks over the eastern Indian Ocean near 90°E, the western Pacific Ocean, and South America near 60°W. However, the good and poor models display only one peak in the Indo-Pacific basin

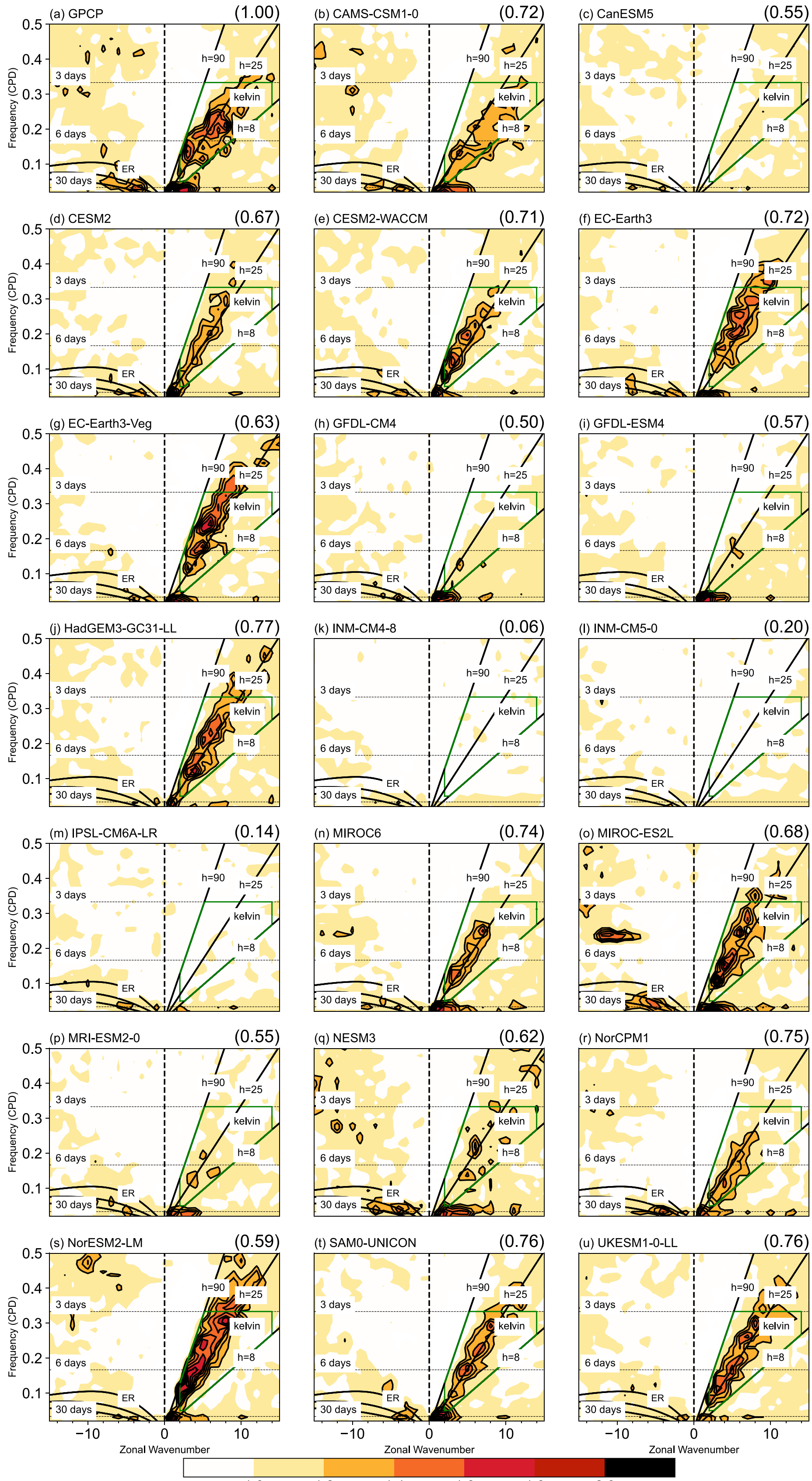

Fig. 2. Similar to Fig. 1, but showing results for all models. The correlation coefficient between each simulation and the observations is displayed in parentheses at the upper right corner of each panel. The coefficient is calculated from the data within the green-filtered domain of the model and observation.

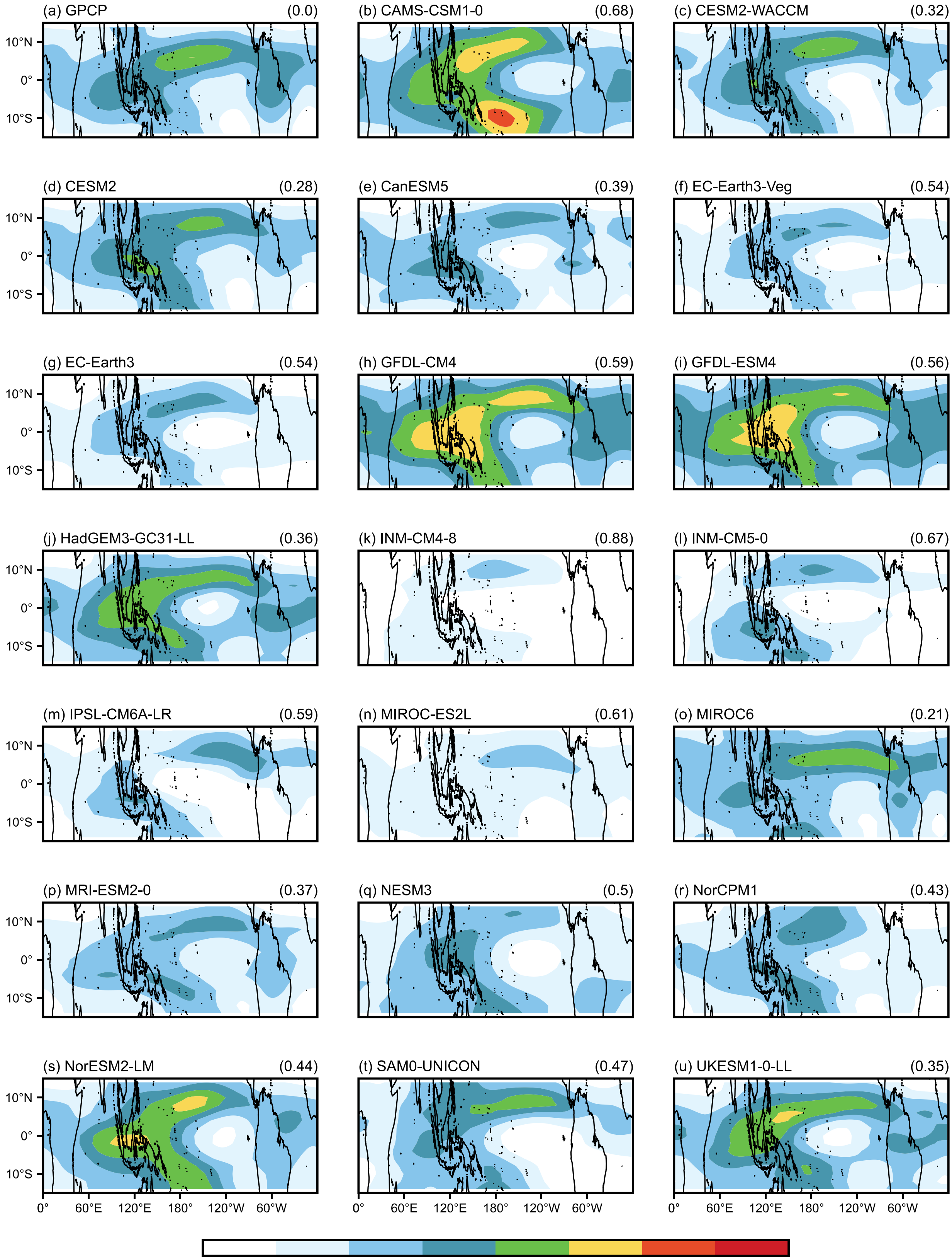

Fig. 3. The standard deviation of CCKW-filtered precipitation anomalies (mm day^{-1}) is shown for (a) GPCP observations and (b)–(u) for each model simulation. The spatial RMSE for each simulation, compared to the observations, is provided in parentheses at the upper right corner of each panel.

with the most active CCKWs occurring near 150°E. Few models can reproduce the vigorous CCKW activity over South America near 60°W, while most models overestimate the CCKW activity near the Maritime Continent. In general, the poor models underestimated the intensity of CCKW activity around the global tropics. However, all models show significant biases in the CCKW simulation in the Maritime Continent and

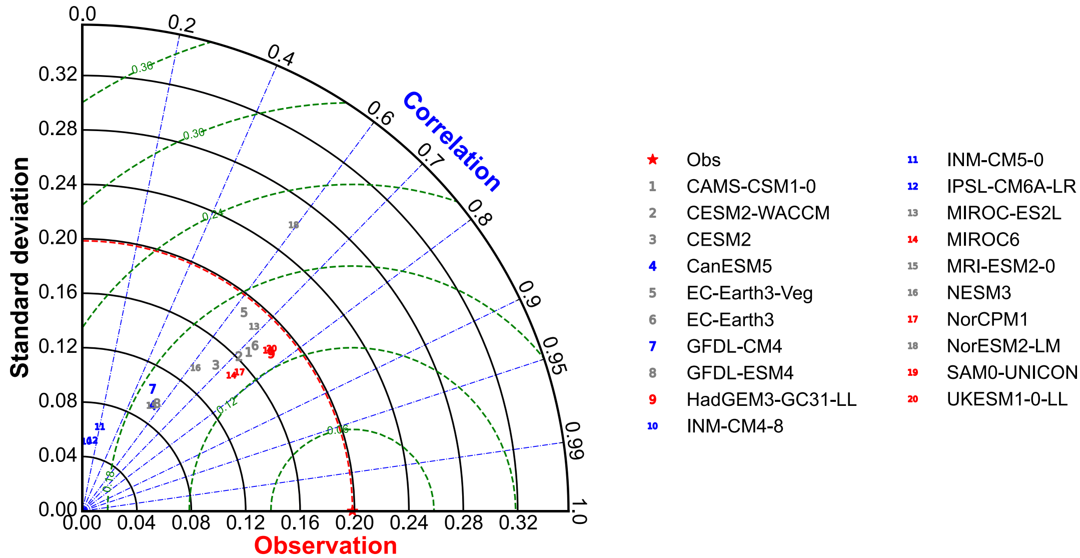

Fig. 4. The Taylor diagram of CMIP6 multiple models, which used GPCP observation as a reference (red). The blue arcs represent correlation coefficients, the black radial indicates standard deviation, and the green concentric arcs correspond to RMSE values.

Table 2
Spatial RMSE and spectral correlation coefficient of good and poor models.

Good Models	Spatial RMSE, Spectral Correlation Coefficient	Poor Models	Spatial RMSE, Spectral Correlation Coefficient
HadGEM3-GC31-LL	(0.36, 0.77)	CanESM5	(0.39, 0.55)
MIROC6	(0.21, 0.74)	GFDL-CM4	(0.59, 0.50)
NorCPM1	(0.43, 0.75)	INM-CM4–8	(0.88, 0.06)
SAM0-UNICON	(0.47, 0.76)	INM-CM5–0	(0.67, 0.20)
UKESM1-0-LL	(0.35, 0.76)	IPSL-CM6A-LR	(0.59, 0.14)

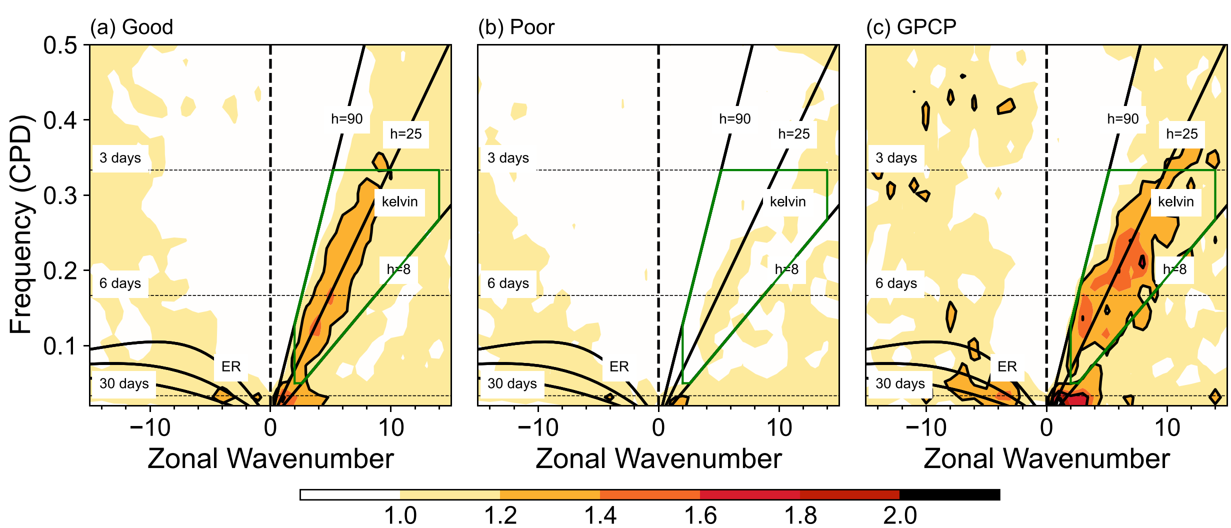

Fig. 5. Same as in Fig. 1, except for (a) the good model average, (b) the poor model average, and (c) GPCP observations.

South America. This issue may be related to the interaction between tropical atmospheric systems and the underlying topography (Birch et al., 2016, 2015; Baranowski et al., 2016; Fukutomi, 2019).

To examine the seasonal variability in simulation accuracy, we further composited the horizontal distribution of CCKW activity for different seasons (Fig. 8). In boreal spring, the observations (Fig. 8c) highlight two key active regions for CCKWs: one located in the central Pacific Ocean and another over the tropical South American continent. Good models generally replicate these observations, albeit with an underestimation of CCKW activity in these two regions and an overestimation of the CCKW signal in the South Pacific (Fig. 8a). Conversely, poor models struggle to capture the signals of strong CCKWs around the global tropics accurately (Fig. 8b). In boreal summer and autumn, good models successfully simulate CCKWs intensities that well-resembles in-situ CCKW activity (Fig. 8d and Fig. 8g), although there were some deviations in the most active regions. For poor models, CCKW signals exist in the tropical northern Pacific with reduced intensity (Fig. 8e and Fig. 8h). Interestingly, during boreal winter, good models overestimated the CCKW activity in the east Indian Ocean region and underestimated that in South America. Moreover, the poor models failed to reproduce CCKWs along the North Pacific ITCZ. These

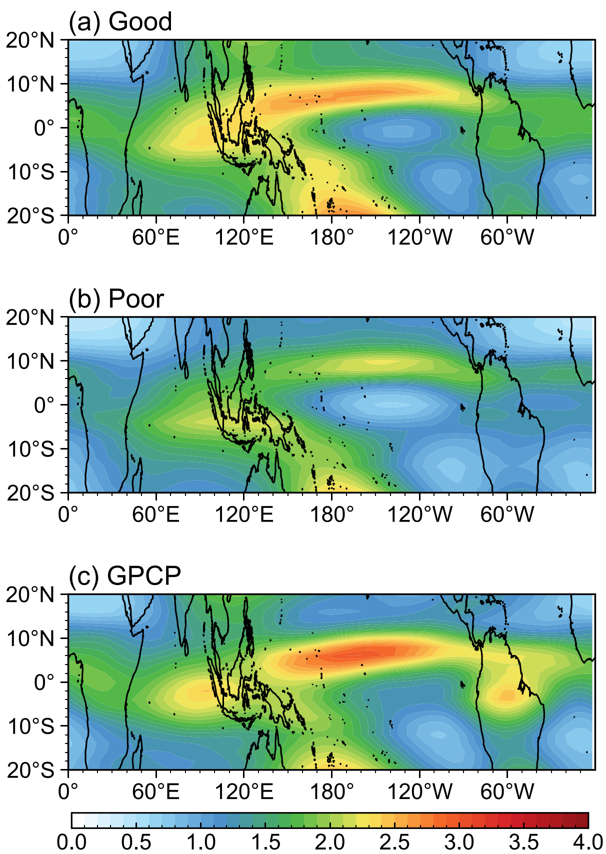

Fig. 6. Standard deviation of CCKW–filtered precipitation (shaded, units: units: mm day^{-1}) for (a) good model average result, (b) poor model average result, and (c) GPCP observation.

results illustrated strong seasonal dependence of the simulation biases of CCKWs, thus the seasonal evolution of CCKWs is required for further investigation.

Figure S1 shows the seasonal spatial correlation between the model-simulated and observed seasonal standard deviations of CCKWs over the tropical belt (20°S-20°N, calculated from Fig. 8). The red bars represent the correlation of Good models, while the blue bars represent that of Poor models. Each bar is labeled with the corresponding correlation coefficient, and the two asterisks indicate passing the 99% statistical significance. Across all seasons (MAM, JJA, SON, DJF), Good models consistently show higher spatial correlation with observations compared to Poor models, with differences ranging from 0.05 to 0.06. This indicates that Good models are more skillful in reproducing the observed spatial patterns of the CCKWs in the tropical region. In addition, it is notable that the overall correlation values tend to be lower during boreal winter (DJF) and spring (MAM) compared to summer (JJA) and autumn (SON), particularly for poor models.

3.3. Evaluation of CCKW seasonal evolution

3.3.1. Seasonal evolution of meridional-mean CCKW activity

Fig. 9 illustrates the seasonal evolution of the meridional mean CCKW activity. Notably, the most intense CCKW activity is observed over the central Pacific around 160°E and South America around 60°W (Fig. 9c). The good models can accurately reproduce the CCKW activity in the central Pacific, including the slight eastward drift of the active region of CCKW from January to May around 160°E, a break of the enhanced CCKW activity during June and September, and a re-intensification starting in October (Fig. 9a). However, the seasonal cycle over South America is misrepresented in good models, and the annual change of the CCKW is significantly weaker in these simulations. The poor models can generally simulate the eastward drift of CCKW activity over the central Pacific during boreal winter and spring. Still, their intensity is remarkably underestimated compared to the observations (Fig. 9b), indicating remarkable biases in these models from January to June. The poor models also failed to reproduce the seasonal evolution of CCKW over South America.

3.3.2. Seasonal evolution of zonal-mean CCKW activity

Fig. 10 illustrates the seasonal cycles of zonal mean CCKW activity. In the observations (Fig. 10c), active CCKWs are concentrated along the equator during boreal winter (January), before intensifying and shifting into the Northern Hemisphere during boreal spring and summer. This shift can be linked to the semiannual variation of Kelvin wave activity over the northern central Pacific and Atlantic, which has also been noted in previous studies (Fig. 9c) (Huang and Huang, 2011). The semiannual variability may be attributed to the seasonal migration of the ITCZ, as the most active convection associated with Kelvin waves tends to follow the latitudinal position of the ITCZ. The seasonal cycles of CCKWs closely follow the patterns of the ITCZ. Regarding CMIP6 simulations, the good models accurately capture the meridional evolution of CCKWs (Fig. 10a), with similar intensity and north–south migration to the observed patterns. Nevertheless, the good models show bias in capturing the peak CCKW activity during March when the observed CCKWs are active near the equator. Generally, the good models produced similar seasonal transitions from Southern to Northern Hemisphere and CCKWs, which is identical to the results in Fig. 8. The poor models illustrate weaker CCKW activity, with an abrupt jump from the Southern Hemisphere to the Northern Hemisphere in March (Fig. 10b), which differs from the observations.

Figure S2 shows the monthly correlation coefficients between the simulated and observed zonal-mean seasonal standard deviation of CCKW (calculated from Fig. 10) for each calendar month over 1997–2014. The multi-month mean correlation is 0.85 for good models and 0.79 for poor models, indicating that poor models exhibit larger bias in simulating the north–south migration of CCKW activity compared to good models. In addition, the simulation bias between the good and poor models in late winter and early spring is significantly lower (correlation coefficient is less than 0.8), reflecting their inadequate simulation performance. There are even cases where the correlation coefficient of the poor model is higher than that of the good model (February–March).

4. Origins of CCKW bias in CMIP6 models

4.1. The mean state in association with the North Pacific ITCZ

The above assessments indicated significant deviation of the CCKW simulation in CMIP6 models. Even good models exert negligible biases in the spatial distribution and seasonal evolution of CCKWs. This discrepancy is even more pronounced in the multi-model averaged results across both classifications. What accounts for this bias in CCKW intensity simulation? As the spatial pattern and seasonal evolution of CCKW activity recall the features of ITCZ, the correlation between CCKW activity and the mean state precipitation in association with the ITCZ in multi-model simulations will be investigated in this section.

Fig. 11 depicts the 18-year mean precipitation in CMIP6 and GPCP observation, illustrating the climatology of ITCZ over the Indo-Pacific basin. Although the CCKW activity follows the spatial distribution of ITCZ, a careful inspection of Figs. 6 and 11 reveals that stronger background precipitation does not necessarily mean a stronger CCKW activity. For instance, both good and poor models tend to overestimate the strength of the North Pacific ITCZ (Fig. 11a,b). However, this region does not correspond to enhanced CCKW activity-especially in poor models, where the overly intensified background precipitation is accompanied by weak simulated CCKW activity (Fig. 6b).

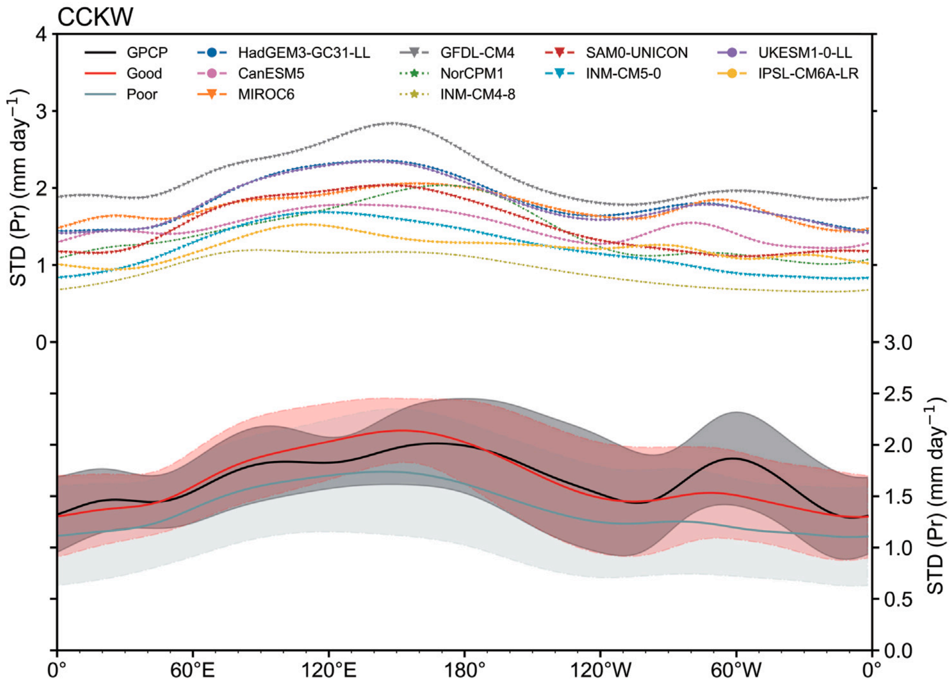

Fig. 7. Zonal distributions of mean standard deviation of precipitation (units: mm day^{-1}) filtered for CCKWs averaged over the latitude from 15°S to 15°N. The dashed lines in the upper panel indicate simulations in different models. The solid lines in the lower panel indicate the multi-model mean of good and poor models, with the shaded area representing the range of ±1.0 standard deviation.

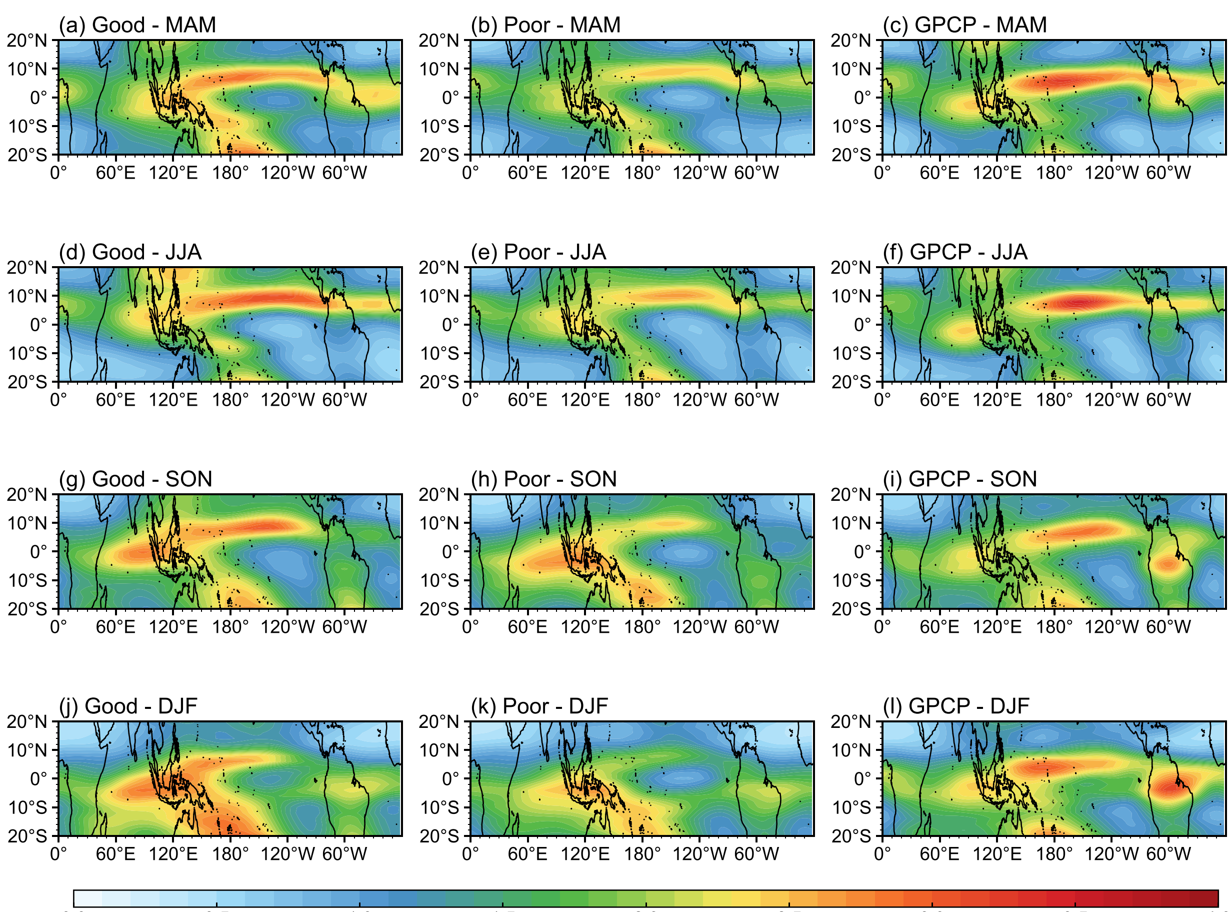

Fig. 8. Same as in Fig. 6, except that it is a simulated performance for each season. The first column represents the standard deviation spatial distribution of the simulated good model average results in the boreal spring, summer, autumn, and winter. The second and third columns are the simulated poor model average results as well as the observed GPCP results, respectively.

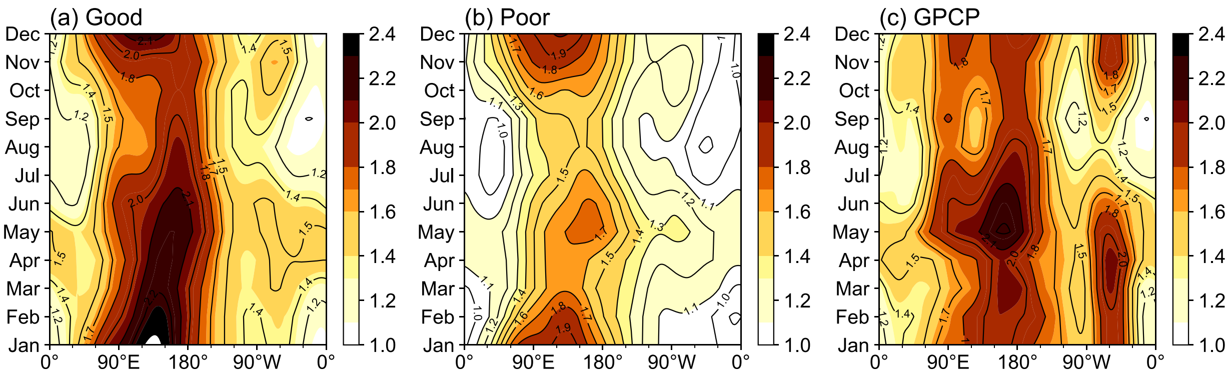

Fig. 9. Zonal evolution of standard deviation of CCKW for (a) good models, (b) poor models, and (c) GPCP observation averaged from 15°S to 15°N.

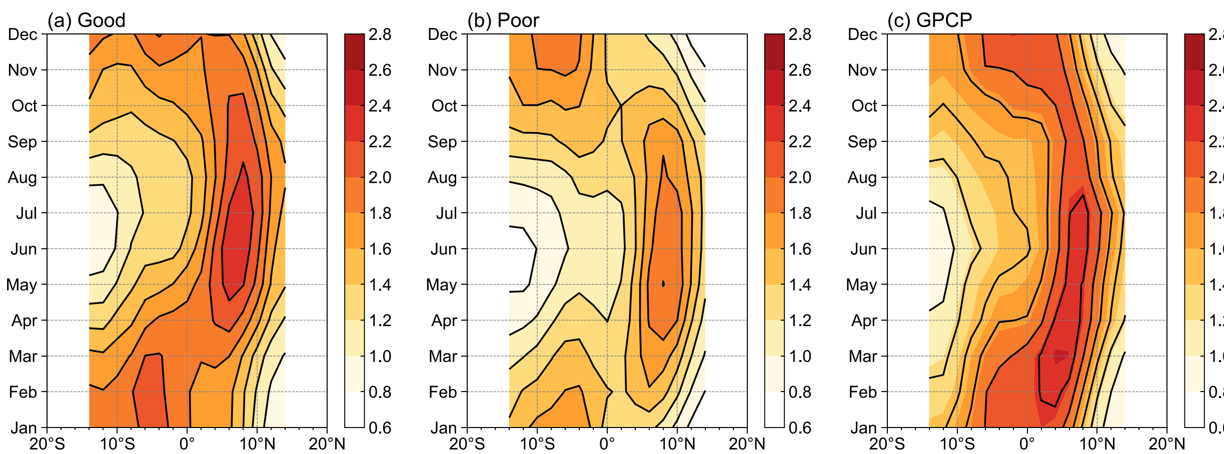

Fig. 10. Meridional evolution of zonal-mean standard deviation of CCKW for (a) good models, (b) poor models, and (c) GPCP observation.

The scatter plot in Fig. 12 illustrates the intermodel correlation between the activity of CCKWs and the strength of the ITCZ across various CMIP6 models. The strength of CCKWs is quantified as the standard deviation of the Kelvin-filtered precipitation in each season, and the bias of CCKWs is calculated as the difference between the model-simulated and observed Kelvin wave strength. Similarly, the background precipitation refers to the seasonal standard deviation of unfiltered monthly mean precipitation (unit: mm day^{-1}), and its bias is defined as the difference between the model and GPCP observations. The correlation between the bias of simulated CCKWs in the Central Pacific and the bias of simulated long-term mean precipitation rate has been calculated. The bias of CCKWs is defined as the difference of the standard deviation of CCKW-filtered precipitation between the observation and simulation, averaged over the region bounded by 0°–15°N and 130°E–90°W. As shown in Fig. 12, a linear relationship with a positive slope is evident between the simulation bias of CCKWs and the simulation bias of background precipitation across all four seasons. In the Northern Hemisphere, the correlation coefficients exceed 0.5 during autumn and winter, which is statistically significant at the 99% and 95% confidence levels based on the Student's t-test. In boreal spring, the correlation coefficients surpass the threshold for the 90% confidence level. Notably, in boreal autumn, the correlation coefficient reached 0.68, suggesting that models with better simulation skills in the mean state precipitation are more likely to produce realistic CCKWs in the equatorial Pacific. In contrast, during boreal summer, simulated CCKW activity shows a weaker correlation with background precipitation. As mentioned above, the simulated spatial distribution of active CCKW also deviates from the observation during boreal summer (Fig. 8c and Fig. 8d). This discrepancy may be attributed to the comprehensive interaction between the backgrounds and the dynamics of CCKWs during the transitional season, which warrants further investigation.

4.2. Potential impact of convective parameterization scheme

Previous studies have shown that simulations of convectively coupled equatorial waves are highly sensitive to convective parameterization (Wang and Schlesinger, 1999; Zhang and McFarlane, 1995; Zhou et al., 2012). Table 3 provides a summary of the convective parameterization schemes, including their deep variants across different models. The majority of models exhibiting a superior correlation coefficient (exceeding 0.4) utilized a mass-flux convection parameterization, except for INM-CM5-0 and INM-CM-8, which employed a convective adjustment parameterization based on Betts (1986). These two models were unable to accurately replicate CCKW activity, as evidenced by their lower correlation coefficients. In the category of poor models, GFDL-CM4 and IPSL-CM6A-LR utilized episodic mixing type mass-flux parameterizations, specifically modified versions of Bretherton et al. (2004) and Emanuel (1991), respectively. Given the limited sample size and the intricate impact of convective parameterization on equatorial wave activity, it is challenging to definitively conclude which types of convective parameterization are more effective for CCKW simulation. However, as indicated in Table 3, models employing mass-flux parameterization appear to have a greater likelihood of simulating realistic CCKW activity.

Convective parameterization influences the activity of tropical variabilities by altering the occurrence and intensity of tropical shallow and deep convection. Numerous studies have indicated that the convective or stratiform precipitation fraction, determined by dividing conditional precipitation by total precipitation, is pivotal in simulating tropical synoptic and intraseasonal variabilities, such as the MJO (Fu and Wang, 2009; Seo and Wang, 2010; Yang et al., 2013; Boyle et al., 2015; Liu et al., 2019). In this section, the convective precipitation fraction is calculated as the ratio of the convective rainfall rate, derived from a

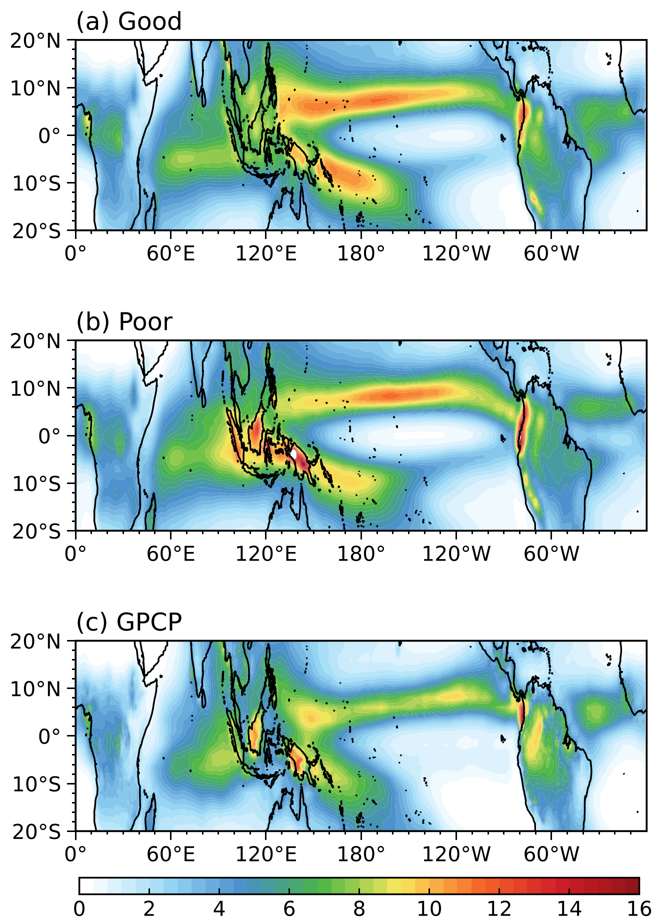

Fig. 11. Spatial distribution of precipitation climatology (shade, units: mm day^{-1}) for (a) good model average, (b) poor model average, and (c) GPCP observation.

convection scheme, to the total precipitation. The total precipitation is the sum of subgrid-scale precipitation from the convection scheme and large-scale precipitation from cloud microphysics schemes.

Fig. 13a illustrates the correlation coefficient of the simulated CCKW concerning the fraction of convective precipitation. The spectral correlation coefficient is calculated from the Kelvin bands of the model and observed spectra window (positive wavenumbers (2–14) and 3–20 day period). Most models are located in the upper half of the diagram (correlation coefficient greater than 0.40), with a wide range of convective precipitation fractions from 0.55 to 0.98. For the three models with correlation coefficients less than 0.40, the convective precipitation fraction ranges from 0.70 to 0.80. The type of convective parameterization used in different models may provide insights into which parameterization scheme is more favorable for CCKW simulation. Except for INM-CM4-8 and INM-CM5-0, which use convective adjustment parameterization, all other models employ mass-flux convective parameterizations. Convective adjustment schemes are typically simple and diagnostic, adjusting temperature and moisture profiles toward a stable state in response to moist instability. In contrast, mass-flux schemes explicitly represent convective plumes and vertical transport through updrafts and downdrafts, with convection driven by the removal of available potential energy (APE) (Ahmed et al., 2020). While adjustment schemes use a prescribed relaxation timescale, mass-flux schemes incorporate convective closures based on quasi-equilibrium assumptions. These models with mass-flux convective parameterizations can be classified into two groups based on the applied convective closure, which exerts significant influence on simulation skill (Li et al., 2023; Suhas and Zhang, 2015). In SAM0-UNICON and IPSL-CM6A-LR, the intensities of deep convection are determined by the dynamical states of the atmospheric boundary layer. For the remaining models, the closures can be treated as variants of the quasi-equilibrium closure, and the intensities of convection are largely constrained, either diagnostically or prognostically, by the moist convective available potential energy produced by large-scale or non-convective processes. Among the models with a correlation coefficient below 0.55, two models adopted convection adjustment parameterization (INM-CM4-8 and INM-CM5-0), and one model (IPSL-CM6A-LR) employed a mass-flux parameterization with a boundary-layer-related closure. As previously mentioned, the limited sample size constrains the possibility of reaching a reliable consensus on why these models fail to simulate realistic CCKWs. However, the present result suggests that models using mass-flux convective parameterization with the quasi-equilibrium closure may be more favorable for the CCKW simulation.

Excluding INM-CM4-8, INM-CM5-0, and IPSL-CM6A-LR, which are distinct from the other models in terms of their convective parameterization schemes, the correlation coefficient of the simulated CCKW exhibits a positive linear relationship with the convective precipitation fraction (Fig. 13b, exceeded the 90% confidence level). These models predominantly employ mass-flux parameterizations. Three models exhibit dominant convective precipitation with a precipitation fraction above 0.95 and the highest simulation skills for CCKWs, with correlation coefficients exceeding 0.75 (UKESM1-0-LL, SAM0-UNICON, and HadGEM3-GC31-LL). This finding suggests a potential strategy for improving CCKW simulation accuracy by increasing convective precipitation intensity through adjustments to mass-flux convective parameterizations in global climate models.

5. Conclusion and discussion

This study evaluates the simulation of CCKWs by 20 coupled climate models from CMIP6. To extract CCKWs, a wavenumber–frequency filter is applied to daily precipitation anomalies after removing the climatological annual cycle. The models were classified into two groups based on the wavenumber–frequency spectrum and the spatial distribution of simulated CCKWs: five models with well-simulated CCKWs (UKESM1-0-LL, SAM0-UNICON, HadGEM3-GC31-LL, MIROC6, NorESM2-LM) and five with poorly-simulated CCKWs (INM-CM5-0, GFDL-CM4, IPSL-CM6A-LR, CanESM5, INM-CM4-8).

The results indicate that the performances deviate remarkably for CMIP6 models in the CCKW simulation. Good models exhibit reliable spectrum and spatial distribution of CCKW activity that are similar to observations, while poor models struggle to reproduce CCKW signals in the wavenumber–frequency diagram and spatial distribution. All models failed to represent the CCKW activity correctly over the Maritime Continent and equatorial South America, implying that the interaction between CCKW and underlying topography, e.g., the Maritime Continent and South America, is urgent to be improved in current earth system models (Birch et al., 2016, 2015; Baranowski et al., 2016; Fukutomi, 2019). The seasonal evolution of CCKWs is generally captured by the good models, yet with non-negligible bias during early boreal spring. Poor models failed to produce the south–north migration of the CCKWs. The horizontal distributions and seasonal cycles of CCKWs resemble those of the ITCZ, implying an inherent interaction between the CCKWs and the North Pacific ITCZ. Scatter plots show a linear relationship between the ITCZ intensity and CCKWs activity, which models with stronger ITCZ favor more active CCKWs, except during boreal spring and summer. The plausible reason needs to be further investigated. In addition, the bias in the simulated Kelvin wave activity centers suggests that current earth system models remain inadequate in accurately representing tropical wave dynamics. These deficiencies underscore the need for improved parameterizations of convection and air-sea interactions to better capture the complex behavior of waves such as CCKWs and other equatorially trapped modes.

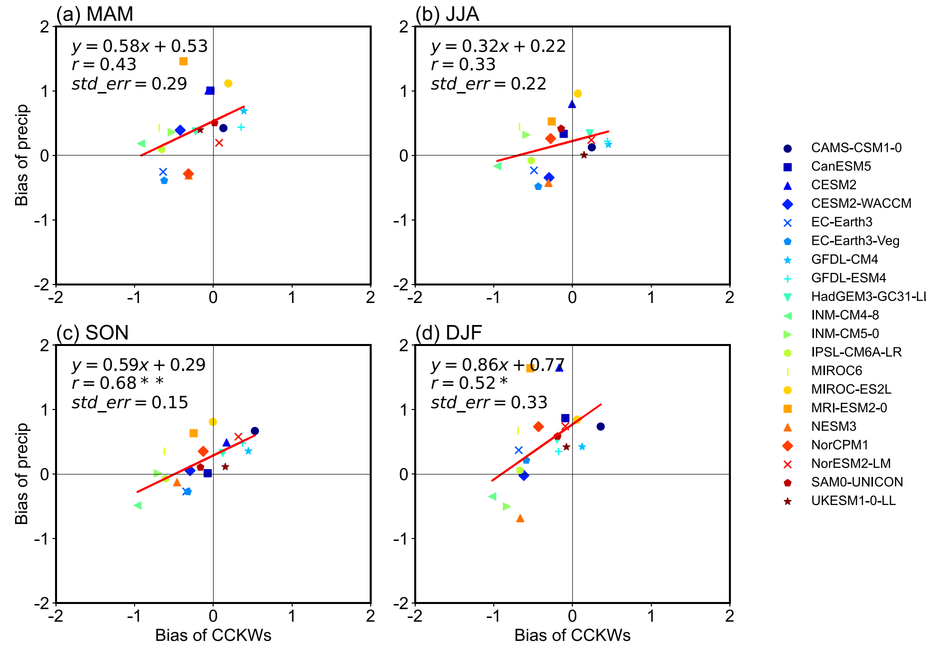

Fig. 12. Scatter plots of the seasonal bias of the CCKWs and background precipitation relative to observations during 1997–2014. The biases are calculated as the difference between each model and the GPCP observation. All calculations are conducted over the domain 0°–15°N, 130°E–90°W for the four seasons: (a) MAM, (b) JJA, (c) SON, and (d) DJF. A single asterisk indicates that it exceeds the 95% confidence level and double asterisks indicate that it exceeds the 99% confidence level.

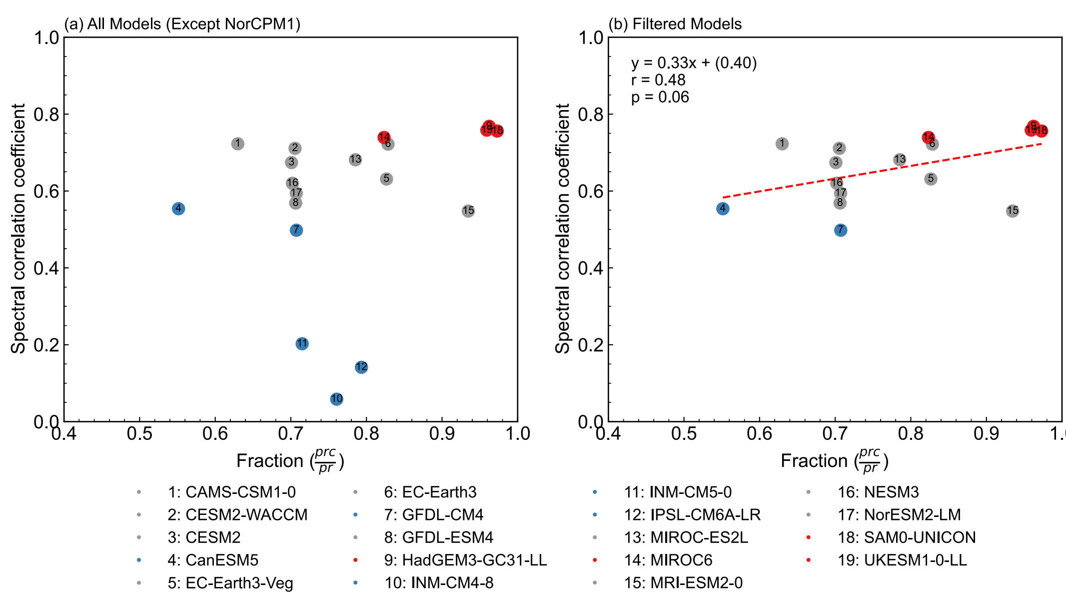

Fig. 13. Scatter plot of spatial–spectral correlation coefficients versus the fraction of convective precipitation in total precipitation. The red points represent the models with good performance, while the blue points represent the models with poor performance. (a) Includes all models, except for NorCPM1, which lacks data on convective precipitation. (b) Models with spectral correlation coefficients below 0.4 were excluded. The red dashed line represents the fitted curve between the correlation coefficient and the fraction.

Most CMIP6 models tend to overestimate the strength of CCKWs in the South Pacific Convergence Zone, particularly pronounced during Northern Hemisphere spring and winter (Fig. 8a-8b, Fig. 8j-8k). Wang and Li (2017) attributed this overestimation to mean precipitation bias when evaluating CCKWs in CMIP5; however, this bias does not appear to have been significantly improved in CMIP6. Interestingly, the bias in CCKW simulations coincides with the overestimation of mean state precipitation. It is interesting to discuss whether this bias is related to the double ITCZ problem, which has not shown significant improvement from CMIP3 to CMIP6 (Si et al., 2021; Tian and Dong, 2020).

Observational evidence suggests a potential connection between the bias of CCKWs and the mean state bias in the Pacific region north of the equator. Areas with strong CCKW activity are typically located within the ITCZ, where maximum variability in the MJO and other high-frequency atmospheric waves coincides with peak seasonal mean convection (Zhang and Dong, 2004; Bui et al., 2023). This study explores the relationship between the CCKW bias and local tropospheric precipitable water, considering that the abundant moisture in the ITCZ may create conditions favorable for enhanced convection and convectively coupled equatorial wave activity. However, the relationship does not show statistical significance (not shown).

Table 3
The list of spectral correlation coefficients and convection parameterizations of 20 CMIP6 models.

Model	Spectral CC	Deep convection Parameterization	Type
HadGEM3-GC31-LL	0.77	Gregory and Rowntree (1990)	Mass-flux model
UKESM1-0-LL	0.76	Gregory and Rowntree (1990)	Mass-flux model
SAM0-UNICON	0.76	Park (2014)	Mass-flux model
NorCPM1	0.75	Zhang and McFarlane (1995)	Mass-flux model
MIROC6	0.74	Chikira and Sugiyama (2010)	Mass-flux model
EC-Earth3	0.72	Bechtold et al. (2014)	Mass-flux model
CAMS-CSM1–0	0.72	Nordeng (1994)	Mass-flux model
CESM2-WACCM	0.71	Zhang and McFarlane (1995)	Mass-flux model
MIROC-ES2L	0.68	Chikira and Sugiyama (2010)	Mass-flux model
CESM2	0.67	Zhang and McFarlane (1995)	Mass-flux model
EC-Earth3-Veg	0.63	Bechtold et al. (2014)	Mass-flux model
NESM3	0.62	Nordeng (1994)	Mass-flux model
NorESM2-LM	0.59	Zhang and McFarlane (1995)	Mass-flux model
GFDL-ESM4	0.57	Zhao et al. (2018)	Mass-flux model
CanESM5	0.55	Zhang and McFarlane (1995)	Mass-flux model
MRI-ESM2–0	0.55	Yoshimura et al. (2015)	Mass-flux model
GFDL-CM4	0.5	Zhao et al. (2018)	Mass-flux model
IPSL-CM6A-LR	0.14	Modified Emanuel (1991)	Mass-flux model
INM-CM5–0	0.2	Betts (1986)	Convective adjustment
INM-CM4–8	0.06	Betts (1986)	Convective adjustment

It should also be noted that the simulation of key modes of tropical variability-including the MJO and the QBO in the stratosphere (Rao et al., 2020, 2023), may be influenced by the representation of CCKWs in earth system models. Due to their vertically propagating nature, CCKWs facilitate energy and momentum exchange between the troposphere and stratosphere, which can contribute to the modulation of the QBO. At the same time, previous studies have pointed out potential dependencies between different waves in general circulation models (GCMs). For example, it has been suggested that there may be a dependency between the MJO and the Kelvin waves in GCMs, such that when the MJO simulation is stronger, the Kelvin waves weaken (Crueger and Stevens, 2015; Kim et al., 2011). Therefore, model deficiencies in simulating CCKWs may contribute to systematic biases in the simulation of both the MJO, QBO (Wang et al., 2023, 2025; Garfinkel et al., 2022), and even the MJO-QBO relationship (Ju et al., 2023, 2025). While the present study focuses on evaluating the characteristics of CCKWs, a natural extension would be to examine whether the CCKWs simulations in models contribute to biases in the representation of MJO and QBO, particularly in light of the absent MJO-QBO connection in CMIP6 simulations (Ju et al., 2023, 2025). Such analysis would be valuable in understanding model limitations in simulating large-scale tropical variability, but is beyond the scope of the current work.

This study also explored the potential impact of convective parameterization on CCKW simulation. Generally, models employing mass-flux convective parameterizations demonstrate strong simulation capabilities for CCKWs. The difference in CCKW simulation skill between mass-flux and convective adjustment schemes likely stems from their underlying physical assumptions. Convective adjustment schemes typically remove atmospheric instability by adjusting temperature and moisture profiles toward a reference state over a prescribed time scale (Betts, 1986). Alternatively, mass-flux schemes eliminate convective instability through vertically eddy transport of heat, moisture, and momentum, governed by assumptions about plume buoyancy, entrainment, and detrainment (Villalba-Pradas and Tapiador, 2022). By explicitly representing vertical convective mass flux, these schemes can better capture the processes of convective triggering, energy exchange, and wave propagation that are essential to sustaining convectively coupled equatorial waves, which might be more appropriate for rapidly evolving, propagating waves in the real atmosphere, such as CCKW. Nevertheless, convective parameterization remains a complex modeling component involving various assumptions (e.g., trigger, closure). Based on the limited samples, models utilizing a convective adjustment scheme or mass-flux convective parameterization seem to encounter challenges in accurately reproducing realistic CCKWs, necessitating further examination. Nonetheless, a positive correlation exists between CCKW simulation skill and the convective precipitation fraction for models with mass-flux convective parameterization. This result is consistent with Baba (2019), who enhanced the CCKW simulation by improving the parameterization scheme and increasing the frequency and development of intense convective clouds. This suggests that the convective precipitation fraction may be one of the factors in the CCKW simulations. The physical mechanisms underlying these results are intriguing and warrant more in-depth investigation in future studies.

CRediT authorship contribution statement

Xianpu Ji: Writing – original draft, Visualization. **Tao Feng:** Writing – review & editing, Validation, Conceptualization. **Ping Huang:** Writing – review & editing, Supervision, Methodology. **Xuhua Cheng:** Writing – review & editing, Supervision, Data curation. **Jianhuang Qin:** Writing – review & editing, Validation, Conceptualization. **Ben Yang:** Writing – review & editing, Formal analysis.

Declaration of competing interest

The authors have no conflicts of interest to declare that are relevant to the content of this article.

Acknowledgments

The authors acknowledge Prof. Dejian Yang for helpful discussion on the spectrum analysis. This study is jointly supported by the National Natural Science Foundation of China (42175063, 42430611) and Jiangsu Provincial Natural Resources Science and Technology Project, China (JSZRKJ202403). The authors sincerely thank the two anonymous reviewers for their constructive comments and helpful suggestions, and the editor for their valuable support, all of which improved the quality of this study.

Appendix A. Supplementary data

Supplementary material related to this article can be found online at https://doi.org/10.1016/j.atmosres.2025.108214.

Data availability

The CMIP6 data used in this study are available at https://pcmdi.llnl.gov/CMIP6/, and the GPCP Precipitation data can be accessed at https://cds.climate.copernicus.eu/datasets.

References

Adames, Á.F., Kim, D., Clark, S.K., Ming, Y., Inoue, K., 2019. Scale analysis of moist thermodynamics in a simple model and the relationship between moisture modes and gravity waves. J. Atmos. Sci. 76 (12), 3863–3881.

Adames, Á.F., Ming, Y., 2018. Interactions between water vapor and potential vorticity in synoptic-scale monsoonal disturbances: Moisture vortex instability. J. Atmos. Sci. 75 (6), 2083–2106.

Ahmed, F., Adames, Á.F., Neelin, J.D., 2020. Deep convective adjustment of temperature and moisture. J. Atmos. Sci. 77 (6), 2163–2186.

Ahn, M.-S., Kim, D., Kang, D., Lee, J., Sperber, K.R., Gleckler, P.J., Jiang, X., Ham, Y.-G., Kim, H., 2020. MJO propagation across the maritime continent: Are CMIP6 models better than CMIP5 models? Geophys. Res. Lett. 47 (11), e2020GL087250.

Baba, Y., 2019. Spectral cumulus parameterization based on cloud-resolving model. Clim. Dyn. 52 (1–2), 309–334.

Baranowski, D.B., Flatau, M.K., Flatau, P.J., Matthews, A.J., 2016. Phase locking between atmospheric convectively coupled equatorial Kelvin waves and the diurnal cycle of precipitation over the maritime continent. Geophys. Res. Lett. 43 (15), 8269–8276.

Bartana, H., Garfinkel, C.I., Shamir, O., Rao, J., 2023. Projected future changes in equatorial wave spectrum in CMIP6. Clim. Dyn. 60 (11–12), 3277–3289.

Bechtold, P., Semane, N., Lopez, P., Chaboureau, J.-P., Beljaars, A., Bormann, N., 2014. Representing equilibrium and nonequilibrium convection in large-scale models. J. Atmos. Sci. 71 (2), 734–753.

Bessafi, M., Wheeler, M.C., 2006. Modulation of south Indian Ocean tropical cyclones by the Madden–Julian oscillation and convectively coupled equatorial waves. Mon. Weather Rev. 134 (2), 638–656.

Betts, A.K., 1986. A new convective adjustment scheme. Part I: Observational and theoretical basis. Q. J. R. Meteorol. Soc. 112 (473), 677–691.

Birch, C.E., Roberts, M.J., Garcia-Carreras, L., Ackerley, D., Reeder, M.J., Lock, A.P., Schiemann, R., 2015. Sea-breeze dynamics and convection initiation: The influence of convective parameterization in weather and climate model biases. J. Clim. 28 (20), 8093–8108.

Birch, C.E., Webster, S., Peatman, S.C., Parker, D.J., Matthews, A.J., Li, Y., Hassim, M.E.E., 2016. Scale interactions between the MJO and the western maritime continent. J. Clim. 29 (7), 2471–2492.

Boyle, J.S., Klein, S.A., Lucas, D.D., Ma, H.-Y., Tannahill, J., Xie, S., 2015. The parametric sensitivity of CAM5's MJO. J. Geophys. Res.: Atmos. 120 (4), 1424–1444.

Bretherton, C.S., McCaa, J.R., Grenier, H., 2004. A new parameterization for shallow cumulus convection and its application to marine subtropical cloud-topped boundary layers. Part I: Description and 1D results. Mon. Weather Rev. 132 (4), 864–882.

Bui, H.X., Li, Y.-X., Maloney, E.D., Kim, J.-E., Lee, S.-S., Yu, J.-Y., 2023. Emergence of Madden–Julian oscillation precipitation and wind amplitude changes in a warming climate. Npj Clim. Atmos. Sci. 6 (1), 22.

Cheng, Y.-M., Dias, J., Kiladis, G., Feng, Z., Leung, L.R., 2023. Mesoscale convective systems modulated by convectively coupled equatorial waves. Geophys. Res. Lett. 50 (10), e2023GL103335.

Chien, M.-T., Kim, D., 2023. Representation of the convectively coupled Kelvin waves in modern reanalysis products. J. Atmos. Sci. 80 (2), 397–418.

Chikira, M., Sugiyama, M., 2010. A Cumulus Parameterization with State-Dependent Entrainment Rate. Part I: Description and Sensitivity to Temperature and Humidity Profiles, vol. 67, no. 7. American Meteorological Society, Boston MA, USA, pp. 2171–2193.

Cho, H.-K., Bowman, K.P., North, G.R., 2004. Equatorial waves including the Madden–Julian oscillation in TRMM rainfall and OLR data. J. Clim. 17 (22), 4387–4406.

Crueger, T., Stevens, B., 2015. The effect of atmospheric radiative heating by clouds on the madden- julian oscillation. JAMES 7 (2), 854–864.

Dias, J., Gehne, M., Kiladis, G.N., Magnusson, L., 2023. The role of convectively coupled equatorial waves in sub-seasonal predictions. Geophys. Res. Lett. 50 (21), e2023GL106198.

Dias, J., Gehne, M., Kiladis, G.N., Sakaeda, N., Bechtold, P., Haiden, T., 2018. Equatorial waves and the skill of NCEP and ECMWF numerical weather prediction systems. Mon. Weather Rev. 146 (6), 1763–1784.

Dias, J., Kiladis, G.N., 2014. Influence of the basic state zonal flow on convectively coupled equatorial waves. Geophys. Res. Lett. 41 (19), 6904–6913.

Emanuel, K.A., 1987. An air-sea interaction model of intraseasonal oscillations in the tropics. J. Atmos. Sci. 44 (16), 2324–2340.

Emanuel, K.A., 1991. A scheme for representing cumulus convection in large-scale models. J. Atmos. Sci. 48 (21), 2313–2329.

Fahrin, F., Gonzalez, A.O., Chrisler, B., Stachnik, J.P., 2024. The relationship between convectively coupled waves and the east Pacific ITCZ. J. Clim. 37 (8), 2565–2583.

Feng, T., Yang, X.-Q., Yu, J.-Y., Huang, R., 2020a. Convective coupling in tropical-depression-type waves. Part I: Rainfall characteristics and moisture structure. J. Atmos. Sci. 77 (10), 3407–3422.

Feng, T., Yu, J.-Y., Yang, X.-Q., Huang, R., 2020b. Convective coupling in tropical-depression-type waves. Part II: Moisture and moist static energy budgets. J. Atmos. Sci. 77 (10), 3423–3440.

Frank, W.M., Roundy, P.E., 2006. The role of tropical waves in tropical cyclogenesis. Mon. Weather Rev. 134 (9), 2397–2417.

Fu, X., Wang, B., 2009. Critical roles of the stratiform rainfall in sustaining the Madden–Julian oscillation: GCM experiments. J. Clim. 22 (14), 3939–3959.

Fukutomi, Y., 2019. Tropical synoptic-scale waves propagating across the maritime continent and northern Australia. J. Geophys. Res.: Atmos. 124 (14), 7665–7682.

Garfinkel, C.I., Gerber, E.P., Shamir, O., Rao, J., Jucker, M., White, I., Paldor, N., 2022. A QBO cookbook: Sensitivity of the quasi-biennial oscillation to resolution, resolved waves, and parameterized gravity waves. JAMES 14 (3), e2021MS002568.

Gregory, D., Rowntree, P.R., 1990. A mass flux convection scheme with representation of cloud ensemble characteristics and stability-dependent closure. Mon. Weather Rev. 118 (7), 1483–1506.

Gruber, A., 1974. The wavenumber-frequency spectra of satellite-measured brightness in the tropics. J. Atmos. Sci. 31 (6), 1675–1680.

Hayashi, Y., 1970. A theory of large-scale equatorial waves generated by condensation heat and accelerating. J. Meteorol. Soc. Jpn. II 48 (2), 140–160.

Herman, M.J., Fuchs, Z., Raymond, D.J., Bechtold, P., 2016. Convectively coupled Kelvin waves: From linear theory to global models. J. Atmos. Sci. 73 (1), 407–428.

Horng, Y.-B., Yu, J.-Y., 2024. On the energetics of convectively coupled Kelvin waves: Contrast between Indian and Pacific basins. Clim. Dyn. 62, 6875–6891.

Huang, P., Chou, C., Huang, R., 2013. The activity of convectively coupled equatorial waves in CMIP3 global climate models. Theor. Appl. Climatol. 112 (3–4), 697–711.

Huang, P., Huang, R., 2011. Climatology and interannual variability of convectively coupled equatorial waves activity. J. Clim. 24 (16), 4451–4465.

Huffman, G.J., Adler, R.F., Morrissey, M.M., Bolvin, D.T., Curtis, S., Joyce, R., McGavock, B., Susskind, J., 2001. Global precipitation at one-degree daily resolution from multisatellite observations. J. Hydrometeorol. 2 (1), 36–50.

Hung, M.-P., Lin, J.-L., Wang, W., Kim, D., Shinoda, T., Weaver, S.J., 2013. MJO and convectively coupled equatorial waves simulated by CMIP5 climate models. J. Clim. 26 (17), 6185–6214.

Jones, P.W., 1999. First- and second-order conservative remapping schemes for grids in spherical coordinates. Mon. Weather Rev. 127 (9), 2204–2210.

Ju, Z., Rao, J., Garfinkel, C.I., Liu, Y., Wang, Y., Lu, Q., 2025. Remote impact of the QBO-MJO on early summer precipitation in eastern Asia: Model evidence from CMIP6. Clim. Dyn. 63 (2), 110.

Ju, Z., Rao, J., Wang, Y., Yang, J., Lu, Q., 2023. Modulation of the intraseasonal variability in early summer precipitation in eastern China by the quasi-biennial oscillation and the Madden–Julian oscillation. Atmos. Chem. Phys. 23 (23), 14903–14918.

Kikuchi, K., Kiladis, G.N., Dias, J., Nasuno, T., 2018. Convectively coupled equatorial waves within the MJO during CINDY/DYNAMO: slow Kelvin waves as building blocks. Clim. Dyn. 50 (11–12), 4211–4230.

Kiladis, G.N., Wheeler, M.C., Haertel, P.T., Straub, K.H., Roundy, P.E., 2009. Convectively coupled equatorial waves. Rev. Geophys. 47 (2), 2008RG000266.

Kim, J.-E., Alexander, M.J., 2013. Tropical precipitation variability and convectively coupled equatorial waves on submonthly time scales in reanalyses and TRMM. J. Clim. 26 (10), 3013–3030.

Kim, D., Sobel, A.H., Kang, I.-S., 2011. A mechanism denial study on the Madden–Julian oscillation: MJO MECHANISM DENIAL STUDY. JAMES 3 (4).

Kuang, Z., 2008. A moisture-stratiform instability for convectively coupled waves. J. Atmos. Sci. 65 (3), 834–854.

Lawton, Q.A., Majumdar, S.J., 2023. Convectively coupled Kelvin waves and tropical cyclogenesis: Connections through convection and moisture. Mon. Weather Rev. 151 (7), 1647–1666.

Le, P.V.V., Guilloteau, C., Mamalakis, A., Foufoula-Georgiou, E., 2021. Underestimated MJO variability in CMIP6 models. Geophys. Res. Lett. 48 (12), e2020GL092244.

Li, X., Zhang, Y., Lin, Y., Peng, X., Zhou, B., Zhai, P., Li, J., 2023. Impact of revised trigger and closure of the double-plume convective parameterization on precipitation simulations over east Asia. Adv. Atmos. Sci. 40 (7), 1225–1243.

Lin, J.-L., Kiladis, G.N., Mapes, B.E., Weickmann, K.M., Sperber, K.R., Lin, W., Wheeler, M.C., Schubert, S.D., Del Genio, A., Donner, L.J., Emori, S., Gueremy, J.-F., Hourdin, F., Rasch, P.J., Roeckner, E., Scinocca, J.F., 2006. Tropical intraseasonal variability in 14 IPCC AR4 climate models. Part I: Convective signals. J. Clim. 19 (12), 2665–2690.

Lindzen, R.D., 1967. Planetary waves on beta planes. Mon. Weather Rev. 95 (7), 441–451.

Lindzen, R.S., 1974. Wave-CISK in the tropics. J. Atmos. Sci. 31 (1), 156–179.

Liu, X., Li, W., Wu, T., Li, T., Gu, W., Bo, Z., Yang, B., Zhang, L., Jie, W., 2019. Validity of parameter optimization in improving MJO simulation and prediction using the sub-seasonal to seasonal forecast model of Beijing climate center. Clim. Dyn. 52 (7–8), 3823–3843.

Lubis, S.W., Jacobi, C., 2015. The modulating influence of convectively coupled equatorial waves (CCEWs) on the variability of tropical precipitation. Int. J. Climatol. 35 (7), 1465–1483.

Lubis, S.W., Respati, M.R., 2021. Impacts of convectively coupled equatorial waves on rainfall extremes in Java, Indonesia. Int. J. Climatol. 41 (4), 2418–2440.

Mapes, B.E., 2000. Convective inhibition, subgrid-scale triggering energy, and stratiform instability in a toy tropical wave model. J. Atmos. Sci. 57 (10), 1515–1535.

Matsuno, T., 1966. Quasi-geostrophic motions in the equatorial area. J. Meteorol. Soc. Jpn. II 44 (1), 25–43.

Mayta, V.C., Adames, Á.F., 2024. The stirring tropics: The ubiquity of moisture modes and moisture–Vortex instability. J. Clim. 37 (6), 1981–1998.

Meehl, G.A., Covey, C., Delworth, T., Latif, M., McAvaney, B., Mitchell, J.F.B., Stouffer, R.J., Taylor, K.E., 2007. The WCRP CMIP3 multimodel dataset: A new era in climate change research. Bull. Am. Meteorol. Soc. 88 (9), 1383–1394.

Neelin, J.D., Held, I.M., Cook, K.H., 1987. Evaporation-wind feedback and low-frequency variability in the tropical atmosphere. J. Atmos. Sci. 44 (16), 2341–2348.

Neena, J., Suhas, E., Jiang, X., 2022. Modulation of the convectively coupled Kelvin waves by the MJO over different domains. J. Clim. 1–39.

Nordeng, T.-E., 1994. Extended versions of the convective parametrization scheme at ECMWF and their impact on the mean and transient activity of the model in the tropics. ECMWF Tech. Memo. (206), 41.

Park, S., 2014. A unified convection scheme (UNICON). Part I: Formulation. J. Atmos. Sci. 71 (11), 3902–3930.

Peyrillé, P., Roehrig, R., Sanogo, S., 2023. Tropical waves are key drivers of extreme precipitation events in the central sahel. Geophys. Res. Lett. 50 (20), e2023GL103715.

Rao, J., Garfinkel, C.I., Ren, R., Wu, T., Lu, Y., Chu, M., 2023. Projected strengthening impact of the quasi-biennial oscillation on the southern hemisphere by CMIP5/6 models. J. Clim. 36 (16), 5461–5476.

Rao, J., Garfinkel, C.I., White, I.P., 2020. How does the quasi-biennial oscillation affect the boreal winter tropospheric circulation in CMIP5/6 models? J. Clim. 33 (20), 8975–8996.

Roundy, P.E., 2008. Analysis of convectively coupled Kelvin waves in the Indian Ocean MJO. J. Atmos. Sci. 65 (4), 1342–1359.

Roundy, P.E., 2012. Observed structure of convectively coupled waves as a function of equivalent depth: Kelvin waves and the Madden–Julian oscillation. J. Atmos. Sci. 69 (7), 2097–2106.

Roundy, P.E., Frank, W.M., 2004. A climatology of waves in the equatorial region. J. Atmos. Sci. 61 (17), 2105–2132.

Schreck, C.J., 2015. Kelvin waves and tropical cyclogenesis: A global survey. Mon. Weather Rev. 143 (10), 3996–4011.

Senior, N.V., Matthews, A.J., Webber, B.G.M., Webster, S., Jones, R.W., Permana, D.S., Paski, J.A.I., Fadila, R., 2023. Extreme precipitation at padang, sumatra triggered by convectively coupled Kelvin waves. Q. J. R. Meteorol. Soc. 149 (755), 2281–2300.

Seo, K.-H., Wang, W., 2010. The Madden–Julian oscillation simulated in the NCEP climate forecast system model: The importance of stratiform heating. J. Clim. 23 (18), 4770–4793.

Si, W., Liu, H., Zhang, X., Zhang, M., 2021. Double intertropical convergence zones in coupled ocean-atmosphere models: Progress in CMIP6. Geophys. Res. Lett. 48 (23), e2021GL094779.

Straub, K.H., Haertel, P.T., Kiladis, G.N., 2010. An analysis of convectively coupled Kelvin waves in 20 WCRP CMIP3 global coupled climate models. J. Clim. 23 (11), 3031–3056.

Straub, K.H., Kiladis, G.N., 2002. Observations of a convectively coupled Kelvin wave in the eastern Pacific ITCZ. J. Atmos. Sci. 59 (1), 30–53.

Straub, K.H., Kiladis, G.N., 2003. The observed structure of convectively coupled Kelvin waves: Comparison with simple models of coupled wave instability. J. Atmos. Sci. 60 (14), 1655–1668.

Suhas, E., Zhang, G.J., 2015. Evaluating convective parameterization closures using cloud-resolving model simulation of tropical deep convection. J. Geophys. Res.: Atmos. 120 (4), 1260–1277.

Takayabu, Y.N., 1994. Large-scale cloud disturbances associated with equatorial waves: Part I: Spectral features of the cloud disturbances. J. Meteorol. Soc. Jpn. II 72 (3), 433–449.

Taylor, K.E., 2001. Summarizing multiple aspects of model performance in a single diagram. J. Geophys. Res.: Atmos. 106 (D7), 7183–7192.

Tian, B., Dong, X., 2020. The double-ITCZ bias in CMIP3, CMIP5, and CMIP6 models based on annual mean precipitation. Geophys. Res. Lett. 47 (8), e2020GL087232.

Tulich, S.N., Kiladis, G.N., 2021. On the regionality of moist Kelvin waves and the MJO: The critical role of the background zonal flow. JAMES 13 (9), e2021MS002528.

Villalba-Pradas, A., Tapiador, F.J., 2022. Empirical values and assumptions in the convection schemes of numerical models. Geosci. Model. Dev. 15 (9), 3447–3518.

Wang, L., Chen, L., 2016. Interannual variation of convectively-coupled equatorial waves and their association with environmental factors. Dyn. Atmos. Oceans 76, 116–126.

Wang, L., Li, T., 2017. Convectively coupled Kelvin waves in CMIP5 coupled climate models. Clim. Dyn. 48 (3–4), 767–781.

Wang, Y., Rao, J., Lu, Y., Ju, Z., 2025. QBO disruption–like events in the China meteorological administration (CMA) climate model. Adv. Atmos. Sci.

Wang, Y., Rao, J., Lu, Y., Ju, Z., Yang, J., Luo, J., 2023. A revisit and comparison of the quasi-biennial oscillation (QBO) disruption events in 2015/16 and 2019/20. Atmos. Res. 294, 106970.

Wang, W., Schlesinger, M.E., 1999. The dependence on convection parameterization of the tropical intraseasonal oscillation simulated by the UIUC 11-layer atmospheric GCM. J. Clim. 12 (5), 1423–1457.

Wang, L., Zhou, T., Li, J., Rong, X., Chen, H., Xin, Y., Su, J., 2019. Convectively coupled equatorial waves simulated by CAMS-CSM. J. Meteorol. Res. 33 (5), 949–959.

Weber, N.J., Kim, D., Mass, C.F., 2021. Convection–Kelvin wave coupling in a global convection-permitting model. J. Atmos. Sci. 78 (4), 1039–1055.

Wheeler, M., Kiladis, G.N., 1999. Convectively coupled equatorial waves: Analysis of clouds and temperature in the wavenumber–frequency domain. J. Atmos. Sci. 56 (3), 374–399.

Wheeler, M., Kiladis, G.N., Webster, P.J., 2000. Large-scale dynamical fields associated with convectively coupled equatorial waves. J. Atmos. Sci. 57 (5), 613–640.

Wolding, B., Dias, J., Kiladis, G., Ahmed, F., Powell, S.W., Maloney, E., Branson, M., 2020. Interactions between moisture and tropical convection. Part I: The coevolution of moisture and convection. J. Atmos. Sci. 77 (5), 1783–1799.

Yamasaki, M., 1969. Large-scale disturbances in the conditionally unstable atmosphere in low latitudes. Pap. Meteorol. Geophys. 20 (4), 289–336.

Yang, G.-Y., Feng, X., Hodges, K., 2023. Seasonal and interannual variation of equatorial waves in ERA5 and GloSea5. Q. J. R. Meteorol. Soc. 149 (752), 1109–1134.

Yang, G.-Y., Hoskins, B., 2013. ENSO impact on Kelvin waves and associated tropical convection. J. Atmos. Sci. 70 (11), 3513–3532.

Yang, G.-Y., Hoskins, B.J., Slingo, J.M., 2011. Equatorial waves in opposite QBO phases. J. Atmos. Sci. 68 (4), 839–862.

Yang, B., Qian, Y., Lin, G., Leung, L.R., Rasch, P.J., Zhang, G.J., McFarlane, S.A., Zhao, C., Zhang, Y., Wang, H., Wang, M., Liu, X., 2013. Uncertainty quantification and parameter tuning in the CAM5 zhang-McFarlane convection scheme and impact of improved convection on the global circulation and climate. J. Geophys. Res.: Atmos. 118 (2), 395–415.

Yang, G.-Y., Slingo, J., Hoskins, B., 2009. Convectively coupled equatorial waves in high-resolution hadley centre climate models. J. Clim. 22 (8), 1897–1919.

Yoshimura, H., Mizuta, R., Murakami, H., 2015. A spectral cumulus parameterization scheme interpolating between two convective updrafts with semi-Lagrangian calculation of transport by compensatory subsidence. Mon. Weather Rev. 143 (2), 597–621.

Zhang, C., Dong, M., 2004. Seasonality in the Madden–Julian oscillation. J. Clim. 17 (16), 3169–3180.

Zhang, G., McFarlane, N.A., 1995. Sensitivity of climate simulations to the parameterization of cumulus convection in the Canadian climate centre general circulation model. Atmos. Ocean. 33 (3), 407–446.

Zhao, M., Golaz, J.-C., Held, I.M., Guo, H., Balaji, V., Benson, R., Chen, J.-H., Chen, X., Donner, L.J., Dunne, J.P., Dunne, K., Durachta, J., Fan, S.-M., Freidenreich, S.M., Garner, S.T., Ginoux, P., Harris, L.M., Horowitz, L.W., Krasting, J.P., Langenhorst, A.R., Liang, Z., Lin, P., Lin, S.-J., Malyshev, S.L., Mason, E., Milly, P.C.D., Ming, Y., Naik, V., Paulot, F., Paynter, D., Phillipps, P., Radhakrishnan, A., Ramaswamy, V., Robinson, T., Schwarzkopf, D., Seman, C.J., Shevliakova, E., Shen, Z., Shin, H., Silvers, L.G., Wilson, J.R., Winton, M., Wittenberg, A.T., Wyman, B., Xiang, B., 2018. The GFDL global atmosphere and land model AM4.0/LM4.0: 2. Model description, sensitivity studies, and tuning strategies. JAMES 10 (3), 735–769.

Zhou, L., B. Neale, R., Jochum, M., Murtugudde, R., 2012. Improved Madden–Julian oscillations with improved physics: The impact of modified convection parameterizations. J. Clim. 25 (4), 1116–1136.